ARTICLE   OPEN

Check for updates

Refining anodic and cathodic dissolution mechanisms: combined AESEC-EIS applied to Al-Zn pure phase in alkaline solution

Junsoo Han [1,3 ✉], Vincent Vivier [2] and Kevin Ogle[1]

In this work, the use of atomic emission spectroelectrochemistry (AESEC) coupled to electrochemical impedance spectroscopy (EIS) is presented as a method of revealing dissolution mechanisms. To illustrate the method, the dissolution kinetics of Al cations from an Al-Zn pure phase (Zn-68 wt.% Al) was investigated in an alkaline solution. In the cathodic potential domain, a nearly direct formation of dissolved Al^{3+} was observed, while in the anodic potential domain the Al dissolution occurred by migration across a $ZnO/Zn(OH)_2$ film. It was demonstrated that this methodology can be applied to a nonstationary system during a potentiostatic experiment for a lower Al content phase (Zn-22 wt.% Al). The nature of the charge transfer mechanisms depended on the applied potential and could be identified by comparing the direct current and alternating current faradaic yield using AESEC-EIS.

npj Materials Degradation (2020)4:19 ; https://doi.org/10.1038/s41529-020-0123-0

INTRODUCTION

Since its introduction to the corrosion field by Epelboin et al.[1], electrochemical impedance spectroscopy (EIS) has proven itself an essential and ubiquitous technique in corrosion research. For steady-state corroding systems, EIS may provide a direct measurement of the corrosion rate[1], and the form of the EIS spectrum may reveal the underlying mechanisms resolved over a wide frequency range of time constants[2]. The advantage of the technique is that it involves only a small amplitude electrochemical perturbation of the system avoiding many of the problems associated with linear scan techniques. The difficulties of EIS alone are the inability to identify the specific faradaic reactions that occur during charge transfer and the requirement of steady-state system. To resolve these difficulties a variety of couplings, such as EIS–Raman spectroscopy[3] have been developed. The nature of the faradaic processes may be revealed by correlating the Raman emission with the modulated current and frequency. The theoretical development of such techniques has been addressed in the development of a generalized EIS transfer function[4].

Atomic emission spectroelectrochemistry (AESEC) provides a direct measurement of elemental dissolution rates[5]. One of the difficulties of this technique is that dissolution may be directly related to a faradaic process, weakly related as in the case of anodic dissolution by way of an oxide intermediate, or unrelated as when dissolution is due to a non-faradaic process. The correlation of electrochemical current transients with dissolution transients is one means of distinguishing between these possibilities as demonstrated by Jiang et al.[6,7] for the dissolution of Zn in the presence of conversion coatings. The coupling of EIS and AESEC allows for a more sophisticated analysis of dissolution kinetics; the oscillating elemental dissolution rates may be related to the oscillating current and low-frequency EIS data may be decomposed into elemental faradaic processes. Further, nonsteady-state systems may be investigated by considering the kinetic data in the time domain. A detailed model for AESEC-EIS was developed by Shkirskiy and Ogle[8], directly correlating the elemental dissolution rate and electrical current for pure Zn at open circuit potential. Zn dissolution in 0.1 M NH₄Cl occurred without any significant intermediate film formation as evidenced by the Zn dissolution rate being in-phase with the alternating current (AC) component of the electrical current. In 0.5 M NaCl solution, no correlation between the AC and the Zn dissolution rate was observed, indicating that oxide film formation and dissolution were decoupled faradaic and non-faradaic processes, respectively. The goal of this article is to extend the previous work to a multielement system and to use the EIS spectra to distinguish different mechanisms of dissolution by taking advantage of the time-resolved measurement of each element of a multielement system that AESEC technique provides.

The Al-Zn alloy system in alkaline solution was considered an ideal system for an early demonstration of the method. The system is industrially significant: Al-Zn alloys are commonly used as galvanic coatings on steel and occur as separate phases in Zn containing Al alloys, such as the 6000 series, and may be exposed to alkaline solution in their lifetime either during surface treatment by alkaline etching, or during corrosion when the cathodic reaction leads to local pH changes. The mechanisms of anodic and cathodic dissolution of multiphase Zn-5 wt.% Al alloy coatings on steel were previously investigated[9,10]. A complex interaction between the Zn and Al was observed; however, interpretation of the mechanisms of these interactions was hindered due to the multiphase nature of the commercial coating material. Therefore, to simplify, we isolated the chemistry of a single phase; the α-phase of Al-Zn (Zn-68 wt.% Al). The anodic dissolution of Al and Zn were investigated as a function of potential in slightly alkaline (pH = 10.1)[11] and alkaline (pH = 12.8)[12] electrolytes. In the latter, the temperature dependence of anodic dissolution was also investigated[13].

[1]Chimie ParisTech, PSL Research University, CNRS, Institut de Recherche Chimie Paris (IRCP), F-75005 Paris, France. [2]Sorbonne Université, CNRS, Laboratoire Interfaces et Systèmes Electrochimiques, LISE, F-75005 Paris, France. [3]Present address: Department of Materials Science and Engineering, University of Virginia, Charlottesville, VA 22904, United States. ✉email: junsoo.hanfr@gmail.com

In summary of these results, three potential domains were identified where the dissolution of the material occurred by very different mechanisms. Based on the individual Zn and Al dissolution rate results and the electrochemical current, it was found that Al underwent a direct, potential independent dissolution mechanism in the cathodic potential domain by reacting with H_2O, and without the formation of a significant intermediate oxide film. Metallic Zn accumulated on the surface in a mechanism of cathodic dealloying. In the anodic domain, Zn was transformed into an oxide film and Al dissolution occurred by ionic transfer across the film. The previous work used the AESEC technique to distinguish the different dissolution mechanisms, such as noise signal and potential dependency of each dissolution rate. As the two mechanisms are very different, it was felt that EIS coupled to AESEC might further confirm these mechanisms and allow a higher degree of precision on the mechanistic details. In this work, a direct comparison between electrical current and elemental dissolution rate of each element during the AESEC-EIS measurement is given. In this way, the dissolution mechanisms of individual alloying elements may be resolved.

RESULTS

Overview of $Al_{5.2}Zn$ mechanisms as a function of potential

The sensitivity of the Al-Zn dissolution mechanism to potential is evident from the AESEC-linear sweep voltammetry (AESEC-LSV) curve of $Al_{5.2}Zn$ (Zn-68 wt.% Al) phase in 0.1 M NaOH solution, shown in Fig. 1. Elemental dissolution rates (j_M) and the convoluted electrical current density (j_e^*) as a function of potential are given with 0.5 mV s^{-1} scan rate. As previously described, the polarization curve shows three distinctive potential domains, to which can be ascribed three unique mechanisms of dissolution. The cathodic dealloying domain occurs between −1.72 V to −1.35 V vs. Hg/HgO, where the dealloyed metallic Zn-enriched layer, Zn(0), is formed by the preferential Al dissolution[12]. It is characterized by an intense Al dissolution rate, j_{Al}, and a Zn dissolution rate, j_{Zn}, close to the detection limit. A direct reaction between Al and H_2O was inferred with significant hydrogen evolution reaction (HER)[14] and accumulation of metallic Zn.
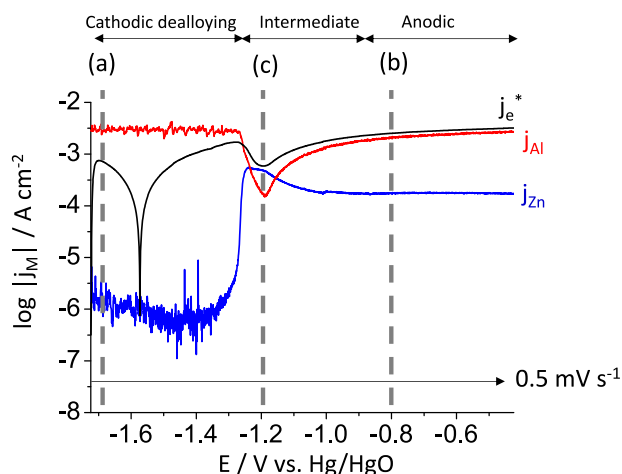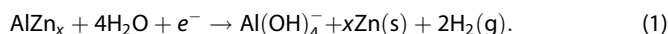
$$AlZn_x + 4H_2O + e^- \rightarrow Al(OH)_4^- + xZn(s) + 2H_2(g). \quad (1)$$

Cathodic dealloying Intermediate Anodic

(a) (c) (b)

Fig. 1 AESEC-LSV curve of $Al_{5.2}Zn$ phase. Elemental current densities (j_M, M = Zn or Al), and convoluted electrical current density (j_e^*) as a function of potential in 0.1 M NaOH, pH = 12.80, Ar deaerated electrolyte at $T = 25$ °C. Vertical dashed lines are selected potential values in the (a): cathodic dealloying, (b): anodic, and (c): intermediate domain.

Al dissolution rate was potential independent and in fact, did not reflect or correlate in anyway with the electrochemical current the magnitude of which was much lower and changed sign during this potential domain.

In the anodic domain (from −0.9 V to −0.4 V vs. Hg/HgO) where a potential independent Zn dissolution is observed, a totally different mechanism is apparent evidenced by the nearly congruent dissolution of Zn and Al, and the significantly decreased amplitude of perturbations in the j_{Al} signal. The direct current (DC) faradaic yield of elemental dissolution may be determined as $\eta_{DC} = j_\Sigma/j_e^*$ when cathodic current contribution is negligible, where $j_\Sigma = j_{Zn} + j_{Al}$. In this case, the dissolution rate follows the electrical current with nearly a 100% DC faradaic yield ($\eta_{DC} = 0.98$) of dissolution. The potential independence of Zn and Al dissolution rates suggests an oxide film formation type of mechanism and indeed, Raman spectroscopy and scanning electron microscopy (SEM) analysis also demonstrated the formation of ZnO layer in this potential domain[11,12].

The elemental dissolution rates in the intermediate domain (from the onset of Zn dissolution −1.35 V vs. Hg/HO to the starting potential of anodic domain −0.90 V vs. Hg/HgO), is more complex. It involves the accumulated metallic Zn-enriched layer that was formed in the cathodic domain by the preferential Al dissolution. At the onset of Zn dissolution, there is a notable decrease in the j_{Al}, that we previously termed a negative correlation effect (NCE) in ref. [12]. The j_{Zn} reached its maximum value in approximately the same potential domain as j_{Al} obtained its minimum value.

AESEC-EIS

To corroborate and gain further insight into the proposed dissolution mechanisms, potentiostatic EIS was performed simultaneously with AESEC in the three potential domains, at potentials indicated as (a), (b), and (c) in Fig. 1. The Nyquist plots are presented in Fig. 2, and the corresponding AESEC-EIS dissolution profiles are given in Fig. 3a–c. The effective oxide capacitance (C_δ) values were determined from the Cole–Cole representation of the complex capacitance curve at high frequency. In this way, the capacitance may be evaluated regardless of any time constant distribution within the oxide film[15]. The capacitance values, the constant phase element (CPE) parameters (α and Q), and the corresponding effective oxide layer thicknesses (δ) for each potential domain are summarized in Table 1.

The cathodic dealloying domain (−1.72 V to −1.35 V vs. Hg/HgO). EIS in the cathodic dealloying domain (Fig. 2a) revealed a single time constant, suggesting that H_2O reduction reaction was the dominate charge transfer reaction. The dissolution profile obtained by AESEC (Fig. 3a) again demonstrates the potential independence of Al dissolution, as the potential cycles at low frequency do not appear as oscillations in the elemental dissolution rates. This is an important conclusion because it indicates that the EIS spectra are revealing information on the interfacial electrochemical processes that may not directly affect the dissolution rate.

The analysis of the high-frequency loop shows a CPE behavior, where $\alpha = 0.73$ and $Q = (1.07 \pm 0.20) \times 10^{-3} \Omega^{-1} cm^{-2} s^{\alpha-1}$, estimated from a graphical analysis[16]. Assuming that this time constant is attributed to a 2D frequency distribution[17], Brug's relationships[18] allow an estimation of the equivalent capacitance from the CPE parameters, in this case the double layer capacitance, $C_{dl} = 191 \mu F cm^{-2}$. This value is about an order of magnitude larger than the expected value for a double layer capacitance and could represent the response of a very thin, perhaps a nonuniform oxide film. It is reasonable to suppose that $Al(OH)_3$ forms as a short-lived intermediate in Reaction 1 as

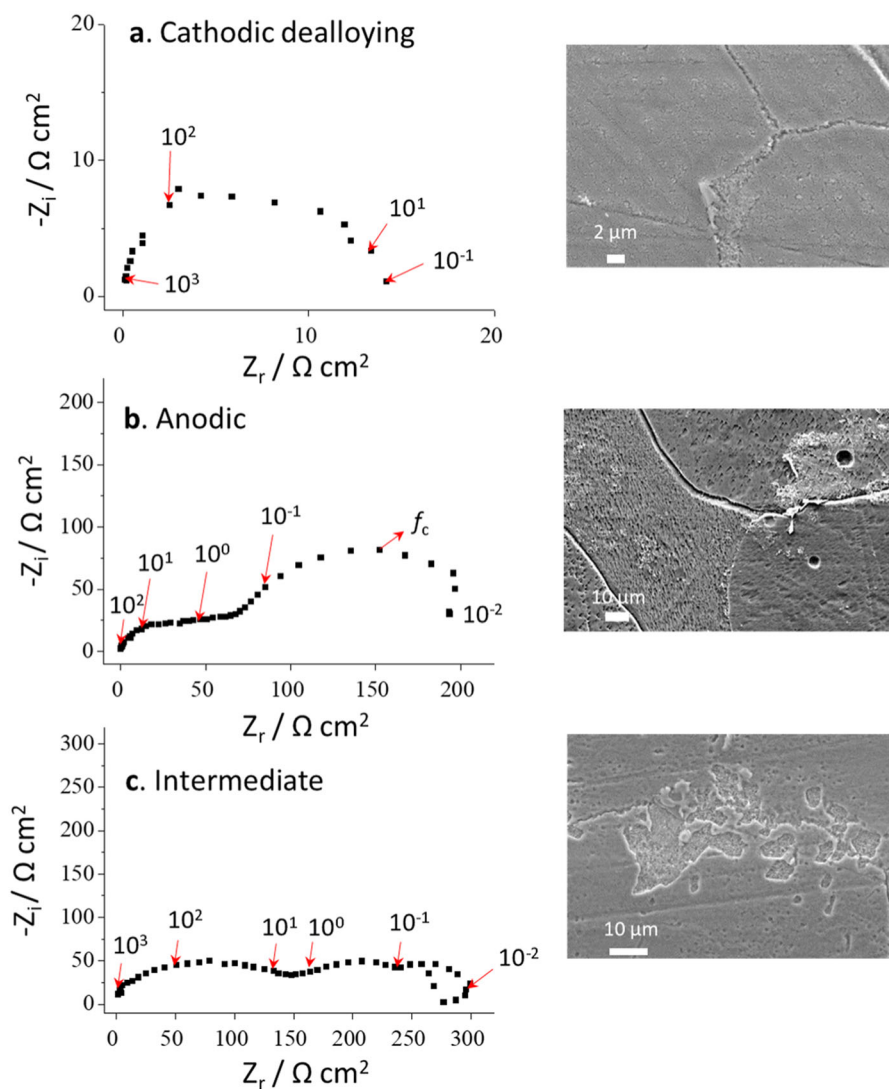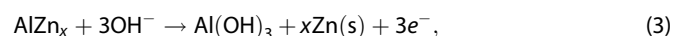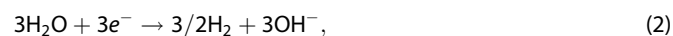**Fig. 2 Nyquist plots at each potential domain.** Potentiostatic EIS of the $Al_{5.2}Zn$ phase at **a** -1.70 V vs. Hg/HgO, **b** -0.80 V vs. Hg/HgO, and **c** -1.20 V vs. Hg/HgO. Arrows are indicating frequency values (Hz). SEM images after the EIS experiment at each potential domain are given.

previously discussed[12,13]. Reaction 1 may be broken down into more elementary steps as follows:

$$3H_2O + 3e^- \rightarrow 3/2H_2 + 3OH^-, \qquad (2)$$

$$AlZn_x + 3OH^- \rightarrow Al(OH)_3 + xZn(s) + 3e^-, \qquad (3)$$

$$Al(OH)_3 + OH^- \rightarrow Al(OH)_4^-. \qquad (4)$$

AESEC directly measures Reaction 4, which involves no electron transfer and in principle should be potential independent. The EIS results indicate that water reduction was potential dependent (Fig. 2a). This confirms the conclusions of ref. [13]; the rate-determining step (RDS) is the dissolution of the $Al(OH)_3$ layer (Reaction 4) as previously reported[19–22]. At steady state, Reactions 3 and 4 must occur at identical rates. The reaction rate is probably determined by the film properties that control the access of H_2O to metallic Al, thereby controlling the cathodic reaction rate (Eq. 2). The presence of the film may not be directly detected by AESEC due to the intense dissolution rate and cathodic current; however, the film was detected indirectly by EIS. The cathodic current resulting from the HER may be determined simply as $j_\Delta = j_e^* - j_\Sigma = j_c$, shown in Fig. 3a.

The anodic domain (-0.9 V to -0.4 V vs. Hg/HgO). In the anodic domain, the polarization curve (Fig. 1) demonstrates that Zn and Al dissolution rates, and the electrochemical current are stable and nearly independent of potential. In the EIS spectrum (Fig. 2b), three time constants are observed. The high-frequency capacitive loop may be attributed to the charge transfer resistance of Zn and/or Al oxidation in parallel with the interfacial capacitance. In this system, independent anodic dissolutions from Zn and Al simultaneously occur at different rate, and thus the admittance is the sum of these contributions. This may explain why the two entangled time constants are observed in the high-frequency domain. The low-frequency loop shows a nearly 45° phase shift that suggests a diffusion process[23,24]. The time constant observed at intermediate frequency ($f = \sim 1$ Hz) is poorly resolved due to overlap with the high- and low-frequency contributions, and will not be discussed.

The high-frequency capacitive loop is flattened and this can be described by a CPE in parallel with the charge transfer resistance. We assume that this CPE is due to the distribution of properties in a thin oxide film[16], for instance, the distribution of resistivity according to a power-law model[25,26]. From the analysis of the complex capacitance calculated from the impedance data[15], the high-frequency limit of the of the capacitance was $C_\delta = 0.65 \pm$
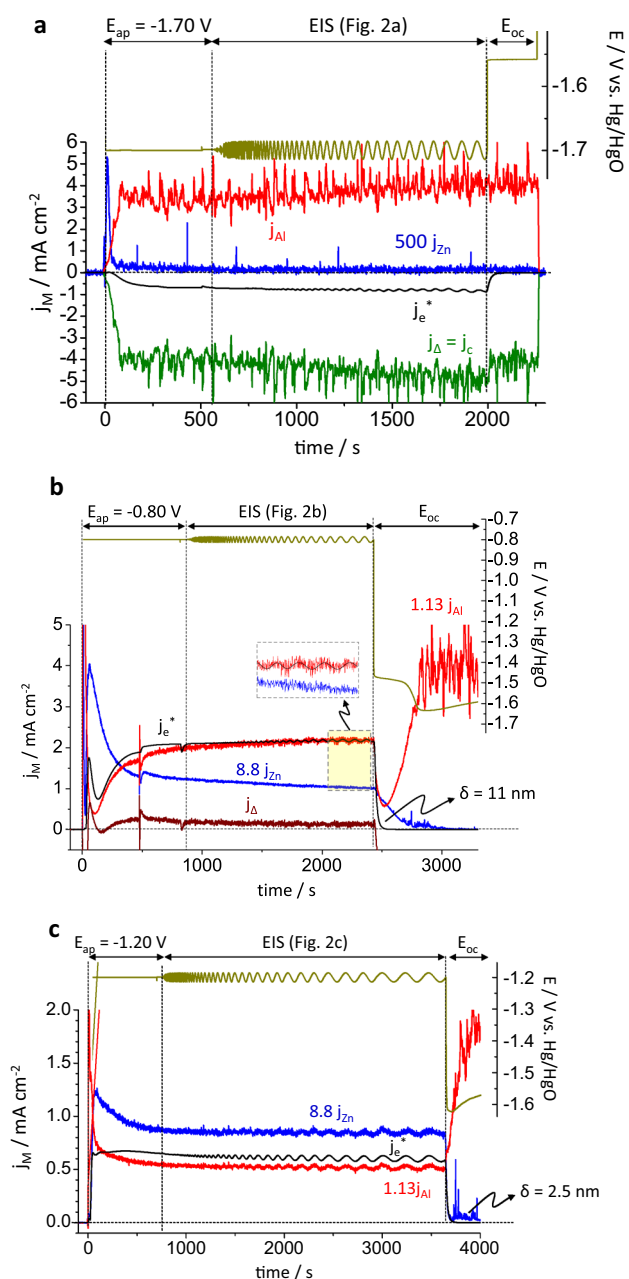
Fig. 3 AESEC-EIS curve of Al$_{5.2}$Zn phase. j_M, j_e^*, and j_Δ during AESEC-EIS measurement in 0.1 M NaOH, Ar deaerated electrolyte including potentiostatic hold (E_{ap}), EIS, and open circuit measurement (E_{oc}). **a** $E_{ap} = -1.70$ V vs. Hg/HgO, **b** $E_{ap} = -0.80$ V vs. Hg/HgO, and **c** $E_{ap} = -1.20$ V vs. Hg/HgO. j_M values are normalized based on the molar composition for **b** and **c**.

0.05 µF cm^{-2}. Such a low value is characteristic of the dielectric response of a thin oxide film. Assuming a dielectric constant $\varepsilon = 8.8 \pm 0.8$ for ZnO (ref. [27]) the thickness of the thin oxide film, δ, formed at the electrode interface is given by:

$$\delta = \varepsilon\,\varepsilon_0 / C_\delta, \qquad (5)$$

where ε_0 is the vacuum permittivity (8.85×10^{-14} F cm^{-1}). This equation yields $\delta = 12 \pm 1$ nm. Such a value confirms the hypothesis that the interfacial capacitance is governed by the thin oxide film contribution (i.e., the double layer capacitance that is in series with the capacitive contribution of the oxide film, has in this case a negligible contribution).

The presence and characteristics of the oxide film may be further refined by consideration of the low-frequency capacitive loop. For the AESEC-EIS (Fig. 3b), very slight oscillations are observed in the Zn and Al dissolution rates at low frequency (magnified curve is given in the inset). The faradaic yield of dissolution for the total current, $\eta_{DC} = 0.96 \pm 0.03$ close to 1, in agreement with ref. [12]. The faradaic yield of the AC component, η_{AC}, is defined as:

$$\eta_{AC} = \text{AC amplitude}\left(j_\sum\right) / \text{AC amplitude}\left(j_e^*\right). \qquad (6)$$

From the data in Fig. 3b, $\eta_{AC} = 1.01 \pm 0.05$, reasonably identical to η_{DC} within experimental error. Note that error bar of η_{AC} was obtained from different frequency domains. It appears to be distributed essentially in the Al dissolution although slight peaks above background are observed for Zn dissolution as well.

The second capacitive loop in Fig. 2b shows a typical diffusion-controlled charge transfer mechanism through an oxide layer[24]. The characteristic frequency, $f_c = 0.032$ Hz, at the apex of the time constant of the diffusion process in the Nernst layer may be expressed as:

$$f_c = 2.51\,D/2\pi\,\delta^2, \qquad (7)$$

where δ is the thickness of the corrosion product, that can be in a first approximation evaluated to be at least the thickness previously obtained from the CPE parameter ($\delta = 12$ nm). The diffusion coefficient may be calculated from Eq. 7, $D = 1.15 \times 10^{-13}$ cm^2 s^{-1}. Such a low value may be due to an underestimated δ value and surface area because the calculation did not consider the porosity of the oxide, as well as the accumulation of corrosion products at the electrode surface. It may be attributed to a diffusion of species inside of a micrometric diffusion layer of corrosion product. In this case, the diffusion and migration caused by the large electric filed inside the film should be taken into account.

Figure 4 shows the oscillation trends of the j_e, j_e^*, j_M, and applied potential (E) at a given frequency of AESEC-EIS result from Fig. 3. To facilitate the comparison, each profile is presented in arbitrary units. The phase shift of j_M and j_e^* vs. E (ϕ_{j_M}) results from the residence time distribution of the flow cell[5], which means that it is

Table 1. The effective capacitance values obtained from Brug's relation[18] (a), complex capacitance curve[15] (b), and (c).

	E_{ap}/V vs. Hg/HgO	C (µF cm^{-2})	α	Q (Ω^{-1} cm^{-2} s$^{\alpha-1}$)	Effective thickness (δ) (nm)	
					EIS	AESEC
(a)	−1.70 V	$C_{dl} = 191$	0.73	$(1.07 \pm 0.20) \times 10^{-3}$	—	
(b)	−0.80 V	$C_\delta = 0.65$	0.78	$(12.6 \pm 0.2) \times 10^{-4}$	12 ± 1	11
(c)	−1.20 V	$C_\delta = 3.3$	0.77	$(4.5 \pm 1.3) \times 10^{-5}$	2.4 ± 0.3	2.5

CPE parameters (α and Q) are provided. The corresponding effective oxide layer thickness (δ) calculated by Eq. 5 and obtained from the AESEC mass-balance are given.
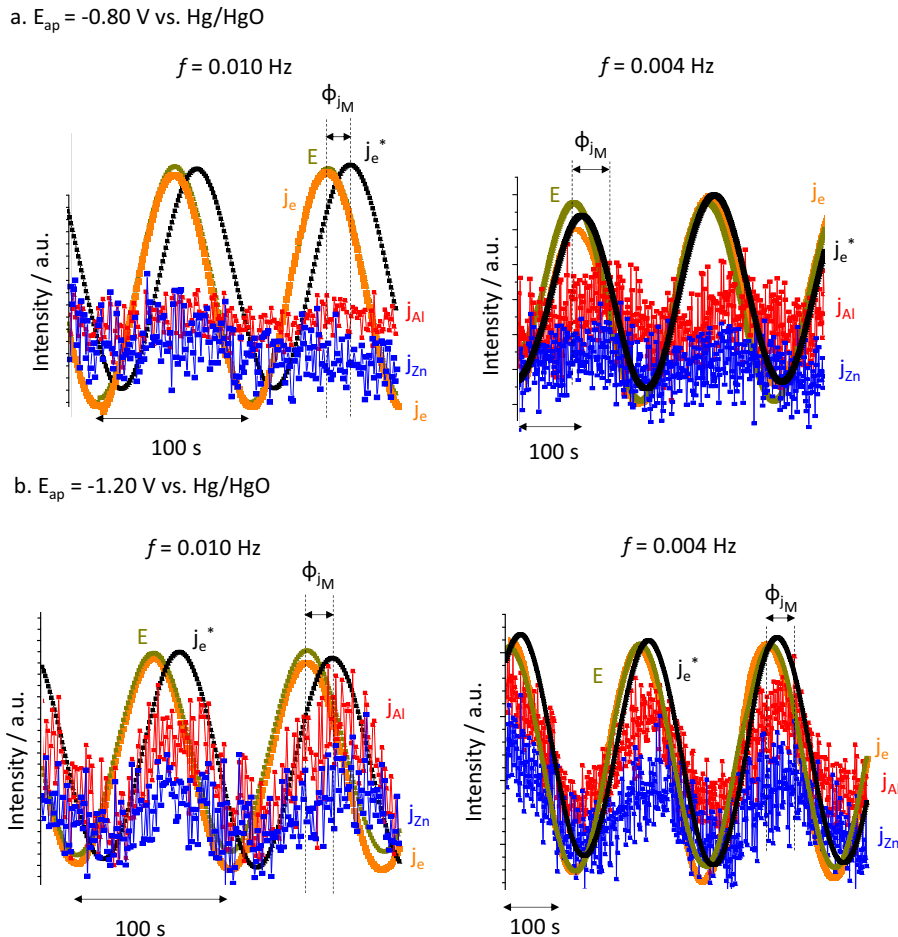
a. E_{ap} = -0.80 V vs. Hg/HgO

b. E_{ap} = -1.20 V vs. Hg/HgO

Fig. 4 The oscillation trends at low-frequency domain. j_M, j_e, j_e^*, and potential (E) as a function of time at a given frequency for **a** $E_{ap} = -0.80$ V vs. Hg/HgO and **b** $E_{ap} = -1.20$ V vs. Hg/HgO from Fig. 3b, c, respectively.

Table 2. The real part impedance measured by the potentiostat (Z_r– R_e), contribution of Zn dissolution (Z_r (j_{Zn})), and Al dissolution (Z_r (j_{Al})).

f (Hz)	Z_r– R_e (Ω cm²)	Z_r (j_{Zn}) (Ω cm²)	Z_r (j_{Al}) (Ω cm²)
$E_{ap} = -0.80$ V vs. Hg/HgO (anodic domain)			
0.010	194	878	19
0.004	192	872	61
$E_{ap} = -1.20$ V vs. Hg/HgO (intermediate domain)			
0.013	305	270	48
0.010	297	274	37
0.008	287	275	37
0.006	279	234	29
0.004	275	266	34

not frequency dependent but time dependent. The actual phase shift between E and j_e (ϕ) was nearly zero in all cases as shown in Fig. 4.

The impedance contribution from each elemental dissolution in real part, Z_r (j_M), is given in Table 2, calculated at each frequency domain as:

$$Z_r(j_M) = (|dE|/|dj_M|)\cos(\phi). \tag{8}$$

For $E_{ap} = -0.80$ V vs. Hg/HgO (Fig. 4a), j_{Zn} oscillation is less evident than at $E_{ap} = -1.20$ V vs. Hg/HgO (Fig. 4b), probably indicating a weak potential dependent Zn dissolution in the anodic potential domain due to Zn-based corrosion product formation. The high Z_r (j_{Zn}) values at $E_{ap} = -0.80$ V vs. Hg/HgO could also be explained by the weak potential dependency of Zn dissolution at this potential. For $E_{ap} = -1.20$ V vs. Hg/HgO, Z_r (j_{Zn}) + Z_r (j_{Al}) ≈ Z_r–R_e, which may indicate that j_{Zn} and j_{Al} contributed to the total impedance with a parallel relationship (R_e is the electrolyte resistance). It is consistent with the previously proposed dissolution model of the Al$_{5.2}$Zn phase, in which Al dissolution occurs through a porous Zn(0) layer in parallel with Zn dissolution[12]. It should be mentioned that the dissolution is not a simple mechanism as it usually involves the adsorbed intermediate species that may result in a delay between the j_e^* and j_M.

The correlation between the AC current and the dissolution rates is highlighted by the Lissajous analysis in Fig. 5a ($E_{ap} = -0.80$ V vs. Hg/HgO) and Fig. 5b ($E_{ap} = -1.20$ V vs. Hg/HgO) at $f = 0.004$ Hz. The j_e^* curve is shown on the top, both for the forward and reverse potential scans. For the j_M vs. E curves in the middle, j_e^* assuming congruent dissolution of Al and Zn are also shown. For example, in Fig. 5a, Al dissolution was congruent as $j_{Al} ≈ (j_e^*/1.13)$, whereas Zn dissolution was not as $j_{Zn} < (j_e^*/8.8)$. The Zn dissolution rate correlated directly with potential although it was less obvious than the Al dissolution rate–potential correlation (also see Fig. 4a). In principle, at this potential, there is no significant cathodic reaction, so we conclude that the AC current is primarily going to the formation and reduction of ZnO or Zn(OH)$_2$.
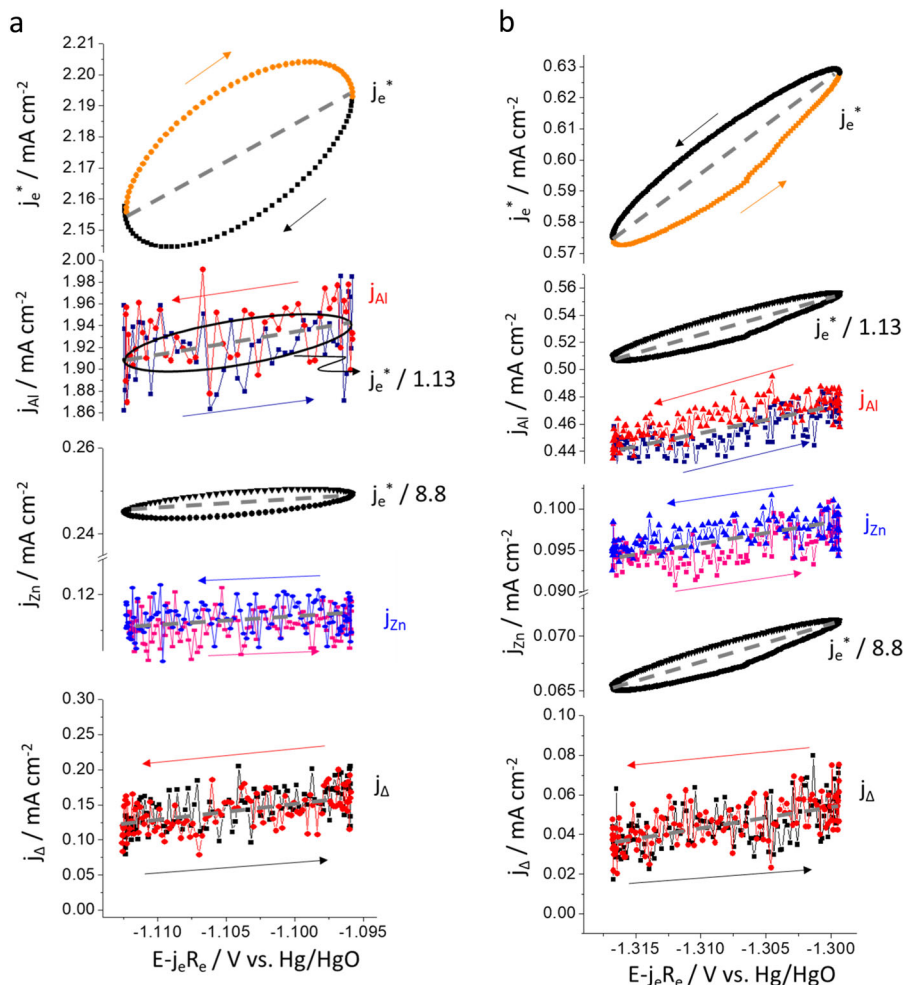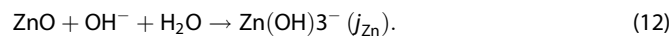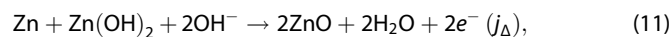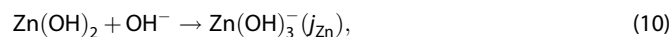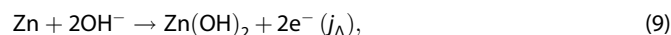
Fig. 5 Elemental Lissajous analysis at $f = 0.004$ Hz. j_e^*, j_{Al}, j_{Zn}, and j_Δ as a function of IR drop compensated applied potential (E–j_eR_e) at **a** $E_{ap} = -0.80$ V vs. Hg/HgO and **b** $E_{ap} = -1.20$ V vs. HgO. One cycle including upper and lower potential scans, indicated by arrows, is given.

It was previously shown that the $\eta_{AC} \approx \eta_{DC} \approx 1$ at $E_{ap} = -0.80$ V vs. Hg/HgO, supporting this assumption. It is worth noting the weak correlation of Zn dissolution rate and potential since the overall faradaic yield of dissolution based on the DC current density and elemental dissolution rates was nearly 100% ($\eta_{DC} = 0.96 \pm 0.03$) at this potential. In this case, it may be concluded that the DC component was due to the dissolution of the corrosion products[6,7,28].

The kinetic parameters for ZnO formation and reduction may be estimated from the j_Δ vs. E Lissajous plot, shown in the bottom of Fig. 5. The Zn dissolution in the anodic potential domain (Fig. 5a) may be a series of elementary reactions as:

$$Zn + 2OH^- \rightarrow Zn(OH)_2 + 2e^- \ (j_\Delta), \tag{9}$$

$$Zn(OH)_2 + OH^- \rightarrow Zn(OH)_3^- \ (j_{Zn}), \tag{10}$$

$$Zn + Zn(OH)_2 + 2OH^- \rightarrow 2ZnO + 2H_2O + 2e^- \ (j_\Delta), \tag{11}$$

$$ZnO + OH^- + H_2O \rightarrow Zn(OH)3^- \ (j_{Zn}). \tag{12}$$

The intermediate species, such as ZnOH or ZnOH$_{ads}$ (refs [29–31]) are not considered as the time scale of the AESEC experiment is too slow to measure these species. The formation rate of Zn(OH)$_2$ or ZnO (j_Δ) is potential dependent (Reactions 9 and 11) given that the Lissajous plot of j_Δ vs. E showed linearity, neglecting the

contribution of cathodic current at this potential. The anodic Tafel slope of j_M (b_a, j_M) may be calculated as:

$$b_{a,jM} = 2.303 \, \Delta E / \ln\left(j_M^+/j_M^-\right), \tag{13}$$

where j_M^+ and j_M^- represent j_M measured at the highest and lowest potential, respectively, obtained from Fig. 5. ΔE is the difference between the highest and lowest potential. $b_{a,j_\Delta} = 94$ mV decade^{-1} and $b_{a,j_{Zn}} = 2350$ mV decade^{-1} are calculated by Eq. 13. It is demonstrated that the formation of ZnO (Reaction 11) is faster than the dissolution (Reaction 12), resulting in the growth of the ZnO layer[12,13].

The quantity of oxide formed during the AESEC-EIS experiment may be estimated by the dissolution profile obtained after releasing the potential to open circuit at the end of the experiment. The $E_{ap} = -0.80$ V vs. Hg/HgO AESEC-EIS profile of Fig. 3b illustrates this idea. At the end of the experiment, the presence of oxide dissolution is indicated by a plateau in the E_{oc} vs. time profile at approximately $E_{oc} = -1.5$ V vs. Hg/HgO. The removal of the oxide and the exposure of the underlying metallic substrate is indicated by the sudden drop in potential to <-1.6 V vs. Hg/HgO. The removal of the oxide film gives rise to a transient dissolution of Zn, which decays steadily but at a rate significantly slower than the residence time distribution associated with the flow cell. The latter is indicated by the drop of the convoluted electrochemical current, j_e^*. Integration of the j_{Zn} yields a thickness of ZnO layer $\delta = 11$ nm, assuming a uniform ZnO layer formation

over the geometrical surface area and a ZnO density of 5.6 g cm^{-3}. This is in the same range as the oxide thickness estimated from EIS of 12 ± 1 nm (Table 1).

The intermediate domain (−1.35 V to −0.9 V vs. Hg/HgO). In the intermediate domain, both j_{Zn} and j_{Al} shows obvious in-phase oscillations, with the low-frequency AC current (Fig. 3c). The EIS response in Fig. 2c shows three capacitive time constants and one inductive loop. An inductive loop has been reported for both Zn and Al dissolution. In the case of Zn, this loop is usually observed in the intermediate frequency range[24,32] whereas for Al, it can be only be seen in the low-frequency domain in an alkaline solution[33,34]. We thus conclude that the inductive loop observed for $f < 10^{-2}$ Hz may be attributed to the relaxation of the surface intermediates involved in the dissolution mechanism of Al and Zn (ref. [35]). The third capacitive loop is similar to the one observed at $E_{ap} = -0.80$ V vs. Hg/HgO and may be ascribed to diffusion processes inside a thin layer. The characteristic frequency is also similar to the previous case in Fig. 2b, confirming that convection–diffusion-controlled mechanism by the flux of the electrolyte in the AESEC experiment.

The second capacitive loop (10^{-1} Hz $< f < 10^{0}$ Hz) was also distributed, and its analysis is complicated by the fact that it is convoluted with other processes at both higher and lower frequency. However, it may be ascribed to Zn dissolution[24]. The high-frequency time constant was analyzed as previously described. From the CPE behavior, the oxide film thickness was estimated at $\delta = 2.4$ nm. The analysis of the high-frequency loop for each potential showed that the thin film formed on the alloy surface has a thickness that strongly depends on the applied potential.

In Fig. 3c, a peak of Zn dissolution is observed after the potential release, albeit a much smaller peak than at $E_{ap} = -0.80$ V vs. Hg/HgO (Fig. 3b). Nevertheless, this peak cannot be unequivocally attributed to oxide dissolution as there is no clearly defined potential plateau following the potential release. Assuming that this peak was due to oxide dissolution, an estimated thickness of 2.5 nm is obtained with the same assumptions as before, in good agreement with that obtained from the EIS analysis of 2.4 ± 0.3 nm (Table 1).

The low-frequency Lissajous plots at $E_{ap} = -1.20$ V vs. Hg/HgO (Fig. 5b) show linear behavior within experimental error, indicating that the elemental dissolution current (j_M) for each species was in-phase with the potential. In this case, the linearity of the Lissajous plots of j_{Zn} and j_Δ is clearly demonstrated, indicating that both reactions are charge transfer limited. The cathodic current would make a negligible contribution to j_e^*, as E_{ap} was ~+400 mV than the zero current potential ($E_{j=0}$). The Zn oxidation reaction may be written by the combination of Reactions 9 and 10 as:

$$Zn + 3OH^- \rightarrow Zn(OH)_3^- + 2e^- \quad (j_{Zn}), \tag{14}$$
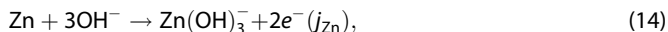
and the formation of the ZnO (j_Δ) is via Reaction 11. $b_{a,j_\Delta} = 68$ mV decade^{-1} and $b_{a,j_{Zn}} = 864$ mV decade^{-1} were obtained by Eq. 13 from Fig. 5b. Given that the Tafel slope of j_{Zn} at $E_{ap} = -1.20$ V vs. Hg/HgO (864 mV decade^{-1}) is lower than that at $E_{ap} = -0.80$ V vs. Hg/HgO (2350 mV decade^{-1}), it could be concluded that the dissolution of Zn is faster in the former case, resulting in a relatively thinner ZnO layer formation.

In this case, both Zn and Al dissolution were not faradaic in that $j_e^*/1.13 \neq j_{Al}$ and $j_e^*/8.8 \neq j_{Zn}$ (Fig. 5b). It showed a significant difference between $\eta_{DC} = 0.92 \pm 0.02$ and $\eta_{AC} = 0.65 \pm 0.03$. It was proposed that the AC component is due to non-faradaic reactions at the metal/oxide interface and the DC component to the faradaic dissolution of the film at the oxide/electrolyte interface[6,7,28]. For the AC case in the intermediate domain, it may be concluded that the formation of the corrosion product would be the RDS, given that $\eta_{DC} \gg \eta_{AC}$, consistent with the Tafel slope analysis. A simplified elemental dissolution at each interface in the
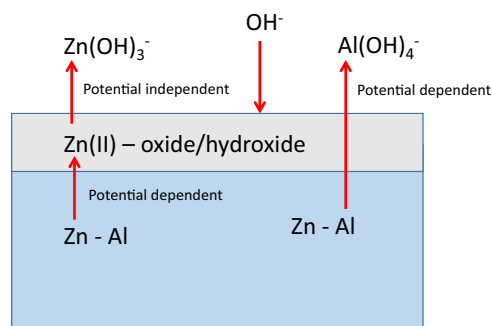

Fig. 6 Schematic dissolution model of Al-Zn phase. Simplified model of elemental dissolution in anodic potential domain at each interface of Al$_x$Zn in 0.1 M NaOH solution.

anodic potential domain is illustrated in Fig. 6. Note that the potential dependent and potential independent mechanisms are observed for two different elements of a material/electrolyte combination. In the previous work with AESEC-EIS, they were observed for pure Zn in two different electrolytes[8].

It is worth noting that j_{Zn} was higher than its congruent dissolution level ($j_e^*/8.8$), whereas j_{Al} was lower than $j_e^*/1.13$. The excess Zn dissolution could lead to a restrained Al dissolution, referenced as the NCE[12].

Al$_{0.7}$Zn (Zn-22 wt.% Al). In this section, we will demonstrate the AESEC-EIS methodology with a nonstationary Zn-Al system during potentiostatic measurement[36]. An AESEC-EIS curve (Fig. 7a), magnified oscillation trends at $f = 0.010$ Hz (Fig. 7b) and a corresponding Nyquist plot (Fig. 7c) for the Al$_{0.7}$Zn (Zn-22 wt.% Al) nominally pure phase at $E_{ap} = -1.36$ V vs. Hg/HgO (i.e., +150 mV from $E_{j=0}$) in the same electrolyte are given. It is demonstrated from Fig. 7a that the elemental dissolution mechanism varied throughout the time period of the experiment at a constant potential. Initially, Zn dissolution was intense at approximately the same level as Al. However, for $t > 2700$ s ($f < 0.005$ Hz), j_{Zn} decreased to under the detection limit and Al dissolution changed from a charge transfer to a chemical dissolution mechanism. The latter is indicated by the disappearing oscillation of j_{Al}, and the significantly increased j_{Al} noise signal resulted from bubble formation by the HER[12,14]. The non-charge transfer Al dissolution mechanism is also revealed in the Nyquist plot (Fig. 7c), where an unambiguous diffusive impedance trend was observed ($\phi = 45°$) in this frequency domain. ZnO/Zn(OH)$_2$ formation and dissolution would occur for $f \geq 0.007$ Hz as Reactions 9–12.

Oscillations were observed in j_{Zn} beginning at a relatively higher frequency domain ($f \approx 0.030$ Hz), where no j_{Al} oscillation was observed. Oscillations in j_{Al} disappeared with the dissolution of ZnO/Zn(OH)$_2$ for $t > 2700$ s, indicating that Al dissolution occurred through this Zn-based corrosion product layer (see also Fig. 6). The phase shift of E vs. j_e (ϕ) was not zero as summarized in Table 3, whereas $\phi \approx 0$ for Al$_{5.2}$Zn (Fig. 4). The measured total impedance was close to the sum of each elemental contribution calculated from Eq. 8, $Z_r - R_e \approx Z_r (j_{Zn}) + Z_r (j_{Al})$, similar to the Al$_{5.2}$Zn in the same potential domain, which can be an indicative of the parallel relationship between Zn and Al dissolution. The phase shift between j_{Zn} and j_{Al} was 180° (Fig. 7b), whereas in-phase relation was monitored for Al$_{5.2}$Zn (Fig. 4). The out-of-phase of j_{Zn} and j_{Al} should have been explained by the fact that Al dissolution is related to the cathodic reaction at open circuit potential[28]. However, this is unlikely in the present work because this phase shift was observed at a relatively positive potential, where the cathodic current contribution is negligible. One possible explanation is that in this potential domain, the slope of the Al dissolution rate–potential curve is negative[36] resulting in a negative low-frequency impedance[37,38].

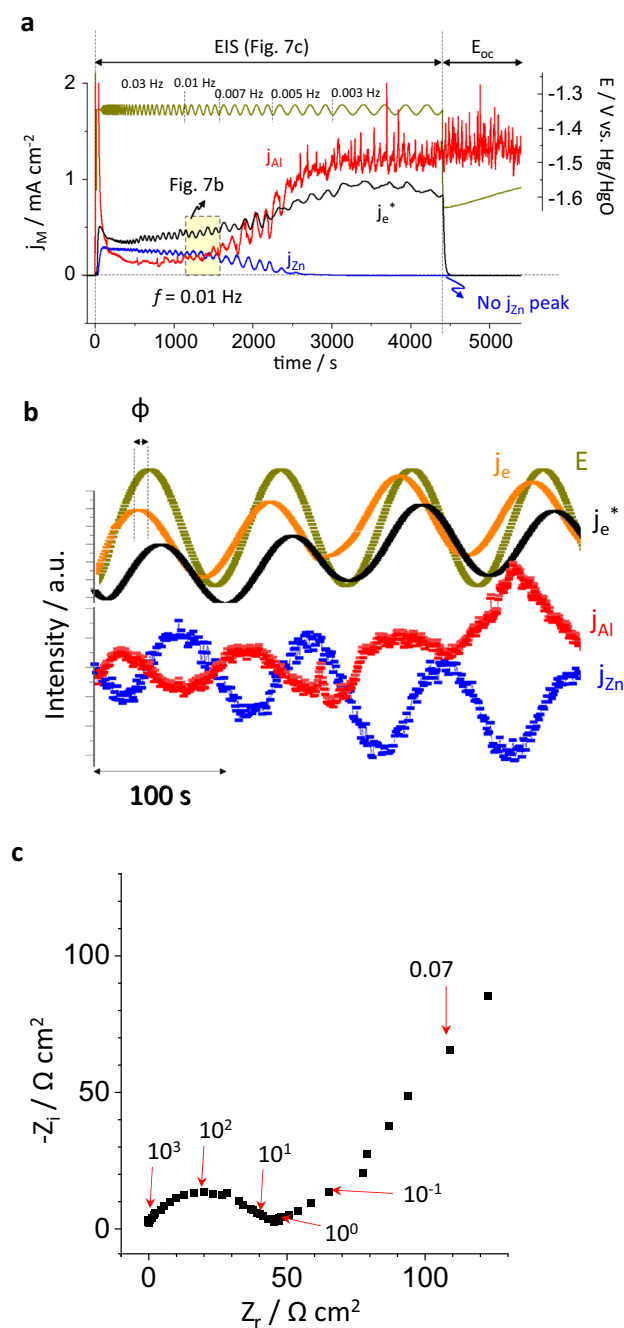For $f \leq 0.007$ Hz, j_{Zn} decreased to under the detection limit as all the previously formed ZnO/Zn(OH)$_2$ dissolves. Previously for Al$_{5.2}$Zn

Fig. 7 AESEC-EIS of Al$_{0.7}$Zn (Zn-22 wt.% Al) phase. a AESEC-EIS curve at $E_{ap} = -1.36$ V vs. Hg/HgO in 0.1 M NaOH, Ar deaerated electrolyte, **b** oscillation trends at $f = 0.010$ Hz from **a**, and **c** corresponding Nyquist plot.

Table 3. The real part of impedance, and ϕ obtained from Fig. 7.

f (Hz)	$Z_r - R_e$ (Ω cm²)	$Z_r (j_{Zn})$ (Ω cm²)	$Z_r (j_{Al})$ (Ω cm²)	ϕ (E vs. j_e)
0.013	101	61	67	−29°
0.010	103	67	75	−32°
0.007	110	66	28	−63°

phase, an obvious Zn dissolution peak was observed during the spontaneous dissolution after the AESEC-EIS experiments in Fig. 3b, c. It was attributed to the residual ZnO/Zn(OH)$_2$ dissolution formed during the potentiostatic experiment. In Fig. 7, no j_{Zn} peak was monitored in E_{oc} indicating that the oxide was completely dissolved near $t = 2700$ s.

DISCUSSION

In this work, we have demonstrated the application of combined AESEC-EIS to identify and quantify different anodic dissolution processes for a multielement system, Al-Zn pure phase in 0.1 M NaOH. The elemental dissolution mechanism at each potential domain was elucidated by the AESEC-EIS technique.

The AESEC method provided immediate information on the elemental dissolution rates and transient behavior, while EIS gave information on the physical properties of intermediate oxide layers and kinetic information for water reduction in the cathodic domain. In the cathodic potential domain ($E_{ap} = -1.70$ V vs. Hg/HgO), Al dissolution was found to be potential independent and occurred with the formation of a negligible oxide layer.

By comparing the DC and AC faradaic yield, information on the localization of charge transfer reactions could be obtained. In the anodic domain ($E_{ap} = -0.80$ V vs. Hg/HgO), $\eta_{DC} \approx \eta_{AC}$ indicating that the formation and dissolution of the corrosion products occur at the nearly same rate, consistent with previous observations[12,13]. In the intermediate domain ($E_{ap} = -1.20$ V vs. Hg/HgO), formation would be the RDS as $\eta_{DC} >> \eta_{AC}$. In the former case, the oxidation of metal occurred through a corrosion product layer. In the latter case, the oxidation occurred directly from the metal/oxide complex. It was further demonstrated by the Tafel slope of j_{Zn} from the elemental Lissajous analysis (Fig. 5). In this way, AESEC-EIS can be utilized to distinguish the different elemental dissolution kinetics. Diffusion processes were identified although the precise origin was not ascertained, i.e., across corrosion product films or within intergranular crevices and pits.

Elemental impedance contribution, $Z_r (j_M)$, demonstrated the potential dependent elemental dissolution model of Al-Zn pure phase proposed in ref. [12]. In the intermediate potential domain, Al dissolution occur through a porous Zn(0)-enriched layer in parallel with Zn dissolution as $Z_r (j_{Zn}) + Z_r (j_{Al}) \approx$ total measured impedance ($Z_r - R_e$).

For Al$_{5.2}$Zn, Al and Zn dissolution rates were in-phase regardless of the applied potential. For Al$_{0.7}$Zn and other low Al content alloys and phases[36], Al and Zn dissolution rates showed a 180° phase shift. However, the origin of the phase shift is not ascertained to the satisfactory level.

METHODS

Materials

Nominally pure phases of Al-Zn (Zn-68 wt.% Al and Zn-22 wt.% Al), provided and characterized by the Department of Metals and Corrosion Engineering, University of Chemistry and Technology, Prague, were investigated in this work. Zn-68 wt.% Al phase is denoted as Al$_{5.2}$Zn and Zn-22 wt.% Al as Al$_{0.7}$Zn, based on their molar compositions to facilitate the congruent dissolution analysis. The chemical composition of these materials were 67.6 wt.% Al and 32.4 wt.% Zn (Al$_{5.2}$Zn), and 21.4 wt.% Al and 78.6 wt.% Zn (Al$_{0.7}$Zn), respectively, measured by atomic absorption spectroscopy. The Al$_{5.2}$Zn contains mainly α-phase of Al with only a trace of η-phase of Zn characterized by X-ray diffraction spectroscopy (XRD). A single β-phase of Al was characterized for Al$_{0.7}$Zn after solution annealing and water quenching. However, this phase decomposes at room temperature into α-phase of Al and η-phase of Zn, also characterized by XRD. All samples were ground with Si-C paper up to P4000 under ethanol, dried with flowing N$_2$ gas then stored in a humidity chamber of 50% relative humidity with saturated Mg(NO$_3$)$_2$·6H$_2$O during 24 h, providing a reproducible native oxide formation on the surface after the sample polishing process[36,39]. All the experiments were performed in a 0.1 M

NaOH (pH = 12.80) at $T = 25\,°C$, prepared from analytical grade materials using deionized water obtained by a Millipore™ system (18.2 MΩ cm). The electrolytes were deaerated by Ar gas for 30 min prior to the tests and maintained during the experiments.

Atomic emission spectroelectrochemistry

The AESEC technique has been described in detail elsewhere[5,40]. The working electrode was in contact with the flowing electrolyte in a specially designed flow cell[5,41] with conventional three-electrode system; a Hg/HgO in 0.1 M NaOH (−165 mV vs. SHE) as a reference electrode and a Pt foil as a counter electrode. The elements released from the working electrode were transported to an Ultima 2 C Horiba Jobin-Yvon inductively coupled plasma atomic emission spectrometer (ICP-AES). The concentrations of Zn and Al were determined from the emission intensity at 213.86 nm (Zn with a Paschen-Runge polychromator) and at 167.08 nm (Al with a monochromator) wavelength, respectively, using standard ICP-AES calibration techniques.

A Gamry Reference 600™ potentiostat was used to perform EIS and LSV. The electrochemical response (namely the electrical current density, j_e, and the electrode potential, E) were recorded in real-time with the elemental dissolution rates, using the analog data acquisition and the software interface (Quantum™, Horiba Jobin-Yvon) of the AESEC technique. The EIS was performed at different potentials from 100 kHz to 0.004 Hz with eight points per decade of frequency and applying a 10 mV$_{rms}$ sinewave perturbation. All the AESEC-EIS experiments were repeated at least three times.

Data analysis of the AESEC technique

The atomic emission intensity at a characteristic wavelength (λ) of the element M, $I_{M,\lambda}$, was recorded by the ICP-AES as a function of time downstream from an electrochemical flow cell. The elemental concentration (C_M) is calculated as:

$$C_M = (I_{M,\lambda} - I_{M,\lambda}^\circ)/\kappa_\lambda, \qquad (15)$$

where $I_{M,\lambda}^\circ$ is the background signal, and is κ_λ the sensitivity factor of M, obtained from a standard ICP calibration method. The elemental dissolution rate (v_M) can be calculated from Eq. 15 with the flow rate of the electrolyte ($f = 2.8$ mL min^{-1}) and the exposed surface area A (1.0 cm^2) as:

$$v_M = fC_M/A. \qquad (16)$$

The v_M was converted to an equivalent elemental current density (j_M) to facilitate comparison with the electrical current density (j_e) measured by the potentiostat, in a relationship with

$$j_M = zFv_M, \qquad (17)$$

where F is the Faraday constant and z is the valance of the dissolving species (Al^{3+}, Zn^{2+}). It is often useful to present j_e^* that represents the measured j_e after a numerical convolution with the residence time distribution in the flow cell (a lognormal distribution), thereby allowing a direct comparison between the instantaneous values of j_e^* and j_M (ref. [5]). Cathodic reactions and the formation of insoluble or slightly soluble species are not directly detected by ICP-AES. If surface charging is neglected, the faradaic component of these hidden processes may be determined by a mass–charge balance as:

$$j_\Delta = j_e^* - j_{Zn} - j_{Al}. \qquad (18)$$

Surface characterization

The sample surface after each potentiostatic AESEC-EIS experiment was characterized by SEM using a Zeiss LEO 1530™ microscope with field emission gun source at 15 keV, and with 15 mm working distance. An equal mix of secondary electron and back-scattered electron detector was used.

DATA AVAILABILITY

The authors declare that the data supporting the findings of this study are available within the paper. The Supplementary Data will be available upon reasonable request.

REFERENCES

1. Epelboin, I., Keddam, M. & Takenouti, H. Use of impedance measurements for the determination of the instant rate of metal corrosion. *J. Appl. Electrochem.* **2**, 71–79 (1972).
2. Keddam, M., Mattos, O. R. & Takenouti, H. Mechanism of anodic dissolution of iron-chromium alloys investigated by electrode impedances - II. Elaboration of the reaction model. *Electrochim. Acta* **31**, 1159–1165 (1986).
3. Wang, X. et al. A new transfer function in electrochemistry: dynamic coupling between Raman spectroscopy and electrochemical impedance spectroscopy. *Electrochim. Acta* **55**, 6299–6307 (2010).
4. Gabrielli, C. & Tribollet, B. A transfer function approach for a generalized electrochemical impedance spectroscopy. *J. Electrochem. Soc.* **141**, 1147–1157 (1994).
5. Ogle, K. Atomic emission spectroelectrochemistry: real time rate measurements of dissolution, corrosion and passivation. *Corrosion* **75**, 1398–1419 (2019).
6. Jiang, L., Wolpers, M., Volovitch, P. & Ogle, K. The degradation of phosphate conversion coatings by electrochemically generated hydroxide. *Corros. Sci.* **55**, 76–89 (2012).
7. Jiang, L., Wolpers, M., Volovitch, P. & Ogle, K. An atomic emission spectroelectrochemical study of passive film formation and dissolution on galvanized steel treated with silicate conversion coating. *Surf. Coat. Tech.* **206**, 3151–3157 (2012).
8. Shkirskiy, V. & Ogle, K. A novel coupling of electrochemical impedance spectroscopy with atomic emission spectroelectrochemistry: application to the open circuit dissolution of zinc. *Electrochim. Acta* **168**, 167–172 (2015).
9. Vu, T. N., Volovitch, P. & Ogle, K. The effect of pH on the selective dissolution of Zn and Al from Zn–Al coatings on steel. *Corros. Sci.* **67**, 42–49 (2013).
10. Vu, T. N., Mokaddem, M., Volovitch, P. & Ogle, K. The anodic dissolution of zinc and zinc alloys in alkaline solution. II. Al and Zn partial dissolution from 5% Al–Zn coatings. *Electrochim. Acta* **74**, 130–138 (2012).
11. Han, J. & Ogle, K. Cathodic dealloying of α-phase Al-Zn in slightly alkaline chloride electrolyte and its consequence for corrosion resistance. *J. Electrochem. Soc.* **165**, C334–C342 (2018).
12. Han, J. & Ogle, K. The anodic and cathodic dissolution of α-phase Zn-68Al in alkaline media. *Corros. Sci.* **148**, 1–11 (2019).
13. Han, J., Thierry, D. & Ogle, K. Temperature dependence of the passivation and dissolution of Al, Zn and α-phase Zn-68Al. *Corrosion* **75**, 68–78 (2019).
14. Han, J. & Ogle, K. Hydrogen evolution and elemental dissolution by combined gravimetric method and atomic emission spectroelectrochemistry. *J. Electrochem. Soc.* **166**, C3068–C3070 (2019).
15. Benoit, M. et al. Comparison of different methods for measuring the passive film thickness on metals. *Electrochem. Acta* **201**, 340–347 (2016).
16. Orazem, M. E., Pébère, N. & Tribollet, B. Enhanced graphical representation of electrochemical impedance data. *J. Electrochem. Soc.* **153**, B129–B139 (2006).
17. Hirschorn, B. et al. Determination of effective capacitance and film thickness from constant-phase-element parameters. *Electrochim. Acta* **55**, 6218–6227 (2010).
18. Brug, G. J., Van Den Eeden, A. L. G., Sluyters-Rehbach, M. & Sluyters, J. H. The analysis of electrode impedance complicated by the presence of a constant phase element. *J. Electroanal. Chem.* **176**, 275–295 (1984).
19. Zhang, J., Klasky, M. & Letellier, B. C. The aluminum chemistry and corrosion in alkaline solutions. *J. Nucl. Mater.* **384**, 175–189 (2009).
20. Chu, D. & Savinell, R. F. Experimental data on aluminum dissolution in KOH electrolytes. *Electrochim. Acta* **36**, 1631–1638 (1991).
21. Moon, S. M. & Pyun, S. I. The corrosion of pure aluminium during cathodic polarization in aqueous solutions. *Corros. Sci.* **39**, 399–408 (1997).
22. Pyun, S. & Moon, S. Corrosion mechanism of pure aluminium in aqueous solution". *J. Solid State Electrochem.* **4**, 267–272 (2000).
23. Cachet, C., Ströder, U. & Wiart, R. The kinetics of zinc electrode in alkaline zincate electrolytes. *Electrochim. Acta* **27**, 903–908 (1982).
24. Cachet, C., De Pauli, C. P. & Wiart, R. The passivation of zinc in slightly alkaline solutions. *Corros. Sci.* **25**, 493–502 (1985).
25. Hirschorn, B. et al. Constant-phase-element behavior caused by resistivity distributions in films: II. Applications. *J. Electrochem. Soc.* **157**, C458–C462 (2010).
26. Hirschorn, B. et al. Constant-phase-element behavior caused by resistivity distributions in films: I. Theory. *J. Electrochem. Soc.* **157**, C452–C457 (2010).
27. Madelung, O., Rössler, U. & Schulz M. *Zinc oxide (ZnO) dielectric constants: Landolt-Börnstein – Group III Condensed Matter*, Vol. 41B (Springer, Berlin Heidelberg, 1999).
28. Shkirskiy, V., Maltseva, A., Ogle, K. & Volovitch, P. Environmental effects on selective dissolution from ZnAlMg alloy under low frequency alternating current perturbations. *Electrochim. Acta* **238**, 397–409 (2017).
29. Bockris, J. O. 'M., Nagy, Z. & Damjanovic, A. On the deposition and dissolution of zinc in alkaline solutions. *J. Electrochem. Soc.* **119**, 285–295 (1975).
30. Cachet, C., Saïdani, B. & Wiart, R. The behavior of zinc electrode in alkaline electrolytes I. A kinetic analysis of cathodic deposition. *J. Electrochem. Soc.* **138**, 678–687 (1991).
31. Thomas, S., Birbilis, N., Venkatraman, M. S. & Cole, I. S. Corrosion of zinc as a function of pH. *Corrosion* **68**, 015009-1-015009-9 (2012).

32. Armstrong, R. D. & Bell, M. F. The active dissolution of zinc in alkaline solution. *Electroanal. Chem. Interf. Electrochem.* **55**, 201–211 (1974).

33. de Wit, J. H. W. & Lenderink, H. J. W. Electrochemical impedance spectroscopy as a tool to obtain mechanistic information on the passive behaviour of aluminium. *Electrochim. Acta* **41**, 1111–1119 (1996).

34. Lnderink, H. J. W., Linden, M. V. D. & de Wit, J. H. W. Corrosion of aluminium in acidic and neutral solutions. *Electrochim. Acta* **38**, 1989–1992 (1993).

35. Gudić, S., Radošević, J. & Kliškić, M. Study of passivation of Al and Al–Sn alloys in borate buffer solutions using electrochemical impedance spectroscopy. *Electrochim. Acta* **47**, 3009–3016 (2002).

36. Han, J. The electrochemistry and dealloying of Zn-Mg/Zn-Al pure phases and their significance for corrosion of Zn-Al-Mg alloys. *PSL Research University,* tel-02860750 (2018).

37. Epelboin, I., Keddam, M. & Lestrade, J. C. Faradaic impedances and intermediates in electrochemical reactions. *Faraday Discuss. Chem. Soc.* **56**, 264–275 (1973).

38. Annergren, I., Keddam, M., Takenouti, H. & Thierry, D. Modeling of the passivation mechanism of Fe-Cr binary alloys from ac impedance and frequency resolved rrde-I. Behavior of Fe-Cr alloys in 0.5M H_2SO_4. *Electrochim. Acta* **41**, 1121–1135 (1996).

39. Stoulil, J. et al. Electrochemical properties of corrosion products formed on Zn-Mg, Zn-Al and Zn-Al-Mg coatings in model atmospheric conditions. *Mat. Corros.* **66**, 777–782 (2015).

40. Ogle, K. & Weber, S. Anodic dissolution of 304 stainless steel using atomic emission spectroelectrochemistry. *J. Electrochem. Soc.* **147**, 1770–1780 (2000).

41. Ogle, K., Lodi, P. & Storhaye, A. Méthode d'analyse d'un échantillon métallique par dissolution de sa surface, et dispositif pour sa mise en œuvre. Patent, FR2689244A1 (1992).

AUTHOR CONTRIBUTIONS

J.H. carried out the AESEC-EIS experiments and coordinated analysis between two techniques. V.V. was responsible for the EIS data interpretation. K.O. conceptualized the AESEC-EIS analysis. All authors contributed to write the paper and revision.

COMPETING INTERESTS

The authors declare no competing interests.

ADDITIONAL INFORMATION

Correspondence and requests for materials should be addressed to J.H.

Reprints and permission information is available at http://www.nature.com/reprints

Publisher's note Springer Nature remains neutral with regard to jurisdictional claims in published maps and institutional affiliations.